Lab on a Chip

PAPER

View Article Online
View Journal | View Issue

Check for updates

Cite this: *Lab Chip*, 2023, **23**, 4092

Capacitive platform for real-time wireless monitoring of liquid wicking in a paper strip†

Isidoro Ruiz-García, [abd] Pablo Escobedo, [abd] Celia E. Ramos-Lorente, [bc] Miguel M. Erenas, [bc] Luis F. Capitán-Vallvey, [bc] Miguel A. Carvajal, [abd] Alberto J. Palma [*abd] and Nuria López-Ruiz [abd]

Received 28th April 2023,
Accepted 20th August 2023

DOI: 10.1039/d3lc00368j

rsc.li/loc

Understanding the phenomenon of liquid wicking in porous media is crucial for various applications, including the transportation of fluids in soils, the absorption of liquids in textiles and paper, and the development of new and efficient microfluidic paper-based analytical devices (μPADs). Hence, accurate and real-time monitoring of the liquid wicking process is essential to enable precise flow transport and control in microfluidic devices, thus enhancing their performance and usefulness. However, most existing flow monitoring strategies require external instrumentation, are generally bulky and unsuitable for portable systems. In this work, we present a portable, compact, and cost-effective electronic platform for real-time and wireless flow monitoring of liquid wicking in paper strips. The developed microcontroller-based system enables flow and flow rate monitoring based on the capacitance measurement of a pair of electrodes patterned beneath the paper strip along the liquid path, with an accuracy of 4 fF and a full-scale range of 8 pF. Additionally to the wired transmission of the monitored data to a computer *via* USB, the liquid wicking process can be followed in real-time *via* Bluetooth using a custom-developed smartphone application. The performance of the capacitive monitoring platform was evaluated for different aqueous solutions (purified water and 1 M NaCl solution), various paper strip geometries, and several custom-made chemical valves for flow retention (chitosan-, wax-, and sucrose-based barriers). The experimental validation delivered a full-scale relative error of 0.25%, resulting in an absolute capacitance error of ±10 fF. In terms of reproducibility, the maximum uncertainty was below 10 nl s^{-1} for flow rate determination in this study. Furthermore, the experimental data was compared and validated with numerical analysis through electrical and flow dynamics simulations in porous media, providing crucial information on the wicking process, its physical parameters, and liquid flow dynamics.

Introduction

Liquid wicking in porous media refers to the process whereby capillary forces draw a liquid into a porous material, driven by its surface tension. The rate of liquid wicking in porous media is dependent on several factors, including the surface tension of the liquid, the pore size and shape of the porous material, the wetting properties of the material, and the geometry and orientation of the porous material.[1–3] This phenomenon is significant in a wide range of applications, including the transport of fluids in soils, the design of microfluidic devices, and the absorption of liquids in textiles and paper.[4–6]

Considerable effort has been invested in comprehending the dynamics of liquid imbibition through porous media, owing to the three-phase complex formation of solid–liquid and –gas interfaces. In 1856, Darcy conducted the first experimental investigation of liquid flow in porous media.[7] His model assumes that flow within a porous medium is driven solely by capillary pressure gradient. In 1921, two researchers established a relationship between the capillary height and the rising time of a liquid in porous media, popularly known as the Lucas–Washburn (LW) equation.[1,2] Various studies have utilized the LW model to understand the physics of liquid wicking in porous media. The LW model scales the liquid wicking distance (L_{lf}) with time (t) as $L_{\mathrm{lf}} \sim t^{1/2}$. However, both Darcy's law and the LW equation make

---

[a] Electronic and Chemical Sensing Solutions (ECsens), CITIC-UGR, Department of Electronics and Computer Technology, University of Granada (UGR), 18071 Granada, Spain. E-mail: ajpalma@ugr.es

[b] Unit of Excellence in Chemistry Applied to Biomedicine and the Environment of the University of Granada, Granada, Spain

[c] Electronic and Chemical Sensing Solutions (ECsens), Department of Analytical Chemistry, University of Granada (UGR), 18071 Granada, Spain

[d] Sport and Health University Research Institute (iMUDS), University of Granada (UGR), 18071 Granada, Spain

† Electronic supplementary information (ESI) available. See DOI: **https://doi.org/10.1039/d3lc00368j**

simplifying assumptions that restrict their applicability. The LW equation assumes a constant capillary diameter throughout the length of the paper, and it does not account for changes in channel geometry or the effects of evaporation. Hence, several modifications have been reported to make both models more accurate. These modifications include the incorporation of different effects such as gravity,[8] liquid evaporation,[9] and fibre swelling,[10–12] among others. Another approach to address this phenomenon is based on Richards's equation.[13] This equation can also be effectively solved with numerical simulators, which have been precisely employed in recent works to shed light on the wicking process in porous media, including several of the aforementioned effects.[14–16] A recent review compiles most of the advances in this area.[17]

Liquid wicking in porous media plays a crucial role in microfluidic paper-based analytical devices (μPADs). The use of μPADs has several advantages over traditional diagnostic techniques, such as being low cost, ease of use, and portable.[18–22] The wicking of the liquid through the porous matrix in μPADs promotes the transport of the sample and facilitates the mixing of the sample with reagents, enabling the detection of target analytes. μPADs have been utilized for a wide range of applications, including detection of infectious diseases, environmental monitoring, and food safety testing.[22] Understanding liquid wicking in porous media is crucial in the development of new and efficient μPADs. By optimizing the properties of the porous material, such as pore size and shape, and the composition of the reagents, the performance of the device can be enhanced, leading to more sensitive and accurate detection of target analytes.[16,23–25]

Flow control is a crucial aspect of μPADs, which rely on capillary forces to manipulate and transport fluids within porous material. Effective flow control is essential to ensure that the liquid flows through the device at the desired rate and reaches the detection zone where the signal is generated. Several strategies have been reported for flow control, including paper strip geometry, mechanical manipulation, chemical modification, and electrical/magnetic/thermal actuators.[5,17] Accurate and real-time flow and flow rate monitoring is essential for useful and practical implementation of these techniques[26] as an alternative to offline flow monitoring methods based on video recording of the wicking process. This ensures precise flow control and therefore improves the performance of microfluidic devices.

External flow sensors are typically employed in systems with active liquid pumping, including close-loop feedbacks, or particle image velocimetry techniques to monitor the flow in microfluidic devices. Although effective, these external solutions are generally bulky and not suitable for portable systems.[27] On the other hand, in the last decade, some integrated flow monitoring strategies, requiring specific fabrication procedures and materials, have been reported based on cantilevers,[28] magnetic composites,[29] piezoelectric nanofibers,[30] optical nanofibers,[31] resonant membranes,[32] and nanoparticles strain sensors on sealed microfluidic channels.[33] Alternatively, techniques based on electrical measurements with conducting electrodes or materials, such as electrical admittance measurements,[34] electrical impedance spectroscopy,[35] electrochemical sensors,[36,37] and piezoresistive membranes,[38] have been presented but require external instrumentation for the electrical magnitude acquisition. A study by the research group of Prof. Delamarche demonstrated a remarkable and inspiring approach for capillary-driven microfluidics in PDMS channels. The channel flow was monitored by measuring the change in a pair of longitudinally patterned metallic electrodes along the hydrophilic flow path while liquid wicking. It produced a dielectric constant change that could be easily detected by capacitive detection. This electronically-microcontrolled setup was provided with a graphical interface and a wireless link to a smartphone for real-time and *in situ* data display and transmission.[26]

In the present work, we have developed a portable electronic platform for real-time and wireless flow monitoring of liquid wicking in paper strips. The performance of this system was evaluated using different water solutions, paper strip geometries, and various chemical valves. Fig. 1 presents a general scheme of our system, which is based on the capacitance measurement of a pair of parallel electrodes patterned beneath the paper strip along the liquid path. These electrodes were designed on a printed circuit board (PCB) along with a capacitance detector and a microcontroller board that includes a Bluetooth link. In addition, experimental capacitive transients were theoretically reproduced with a numerical simulator including both electrical and flow in porous media simulations. The full geometry of the experimental setup was included in the COMSOL Multiphysics software to perform the numerical analysis of the capacitance change of the imbibition process as a function of time. The comparison of experimental and numerical data provides fundamental information about the wicking process in terms of the physical parameters involved, such as dielectric constant, pore size, and permeability; and the flow relevant features, including the dynamics of the length of the liquid front, absorbed liquid mass/volume, and liquid mass/volume flow. To the best of our knowledge, this is the first compact system that enables monitoring of liquid wicking along an entire paper strip, providing physical information about the phenomenon through numerical simulation.

Experimental and numerical procedures

Materials and software

The electronic components were procured from RS Components supplier (Corby, UK). The printed circuit board and the capacitive electrode structure were fabricated using the computer-controlled circuit board plotter LPKF ProtoMat S100 (LPKF Laser & Electronics SE, Garsen, Germany). An

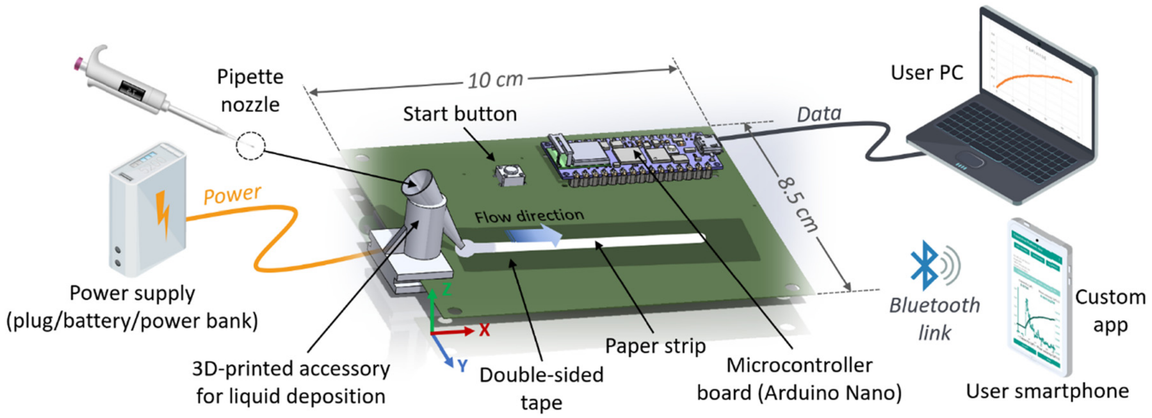

Fig. 1 Overview of the capacitive platform for liquid wicking monitoring.

accessory for a micropipette tip holder was 3D printed with a Creality CR-X 3D printer (Creality, Shenzhen, China) using polylactic acid (PLA) filament. The proposed capacitive sensing platform was validated using a precision LCR meter E4980AL (Keysight Tech., Santa Rosa, CA, USA). The dielectric constants of the paper, both dry and imbibed with purified water, were measured using a 40 Hz to 110 MHz precision impedance analyzer 4294A interfaced to the dielectric material test fixture with parallel plate electrodes, 16451B (Keysight Tech., Santa Rosa, CA, USA). The physical study of the experimental setup, including the surface morphology and texture changes of the paper strip during the wicking process, was carried out using the 3D optical profilometer SNeox (Sensofar, Barcelona, Spain). The confocal technique was configured with ×5, ×20, and ×50 optical objectives, achieving a spatial resolution ranging from 470 to 180 nm. The features of the surface texture standard ISO 25178 were calculated by the profilometer software SensoVIEW 1.9.2. A Xiaomi Redmi Note 11S smartphone (Xiaomi Corporation, Beijing, China) was used for video recording during the validation of the platform, configuration, and real-time results display.

Filter paper Whatman grade 1 (Merck KGaA, Sant Louis, USA) was selected for all experiments of this work. Different paper strip shapes were obtained using a laser cutting machine (Rayjet 50 Laser Engraver, Austria). Hydrophobic double-sided adhesive tape Tesa 64621 (Tesa, Hamburg, Germany) was used to affix the paper strip to the capacitive electrodes. Purified water was produced by a TKA Microlab type II (TKA Wasseraufbereitungssysteme GmbH, Niederelbert, Germany) for the experiments to evaluate the sensing platform's performance. High molecular weight chitosan, NaCl, and sucrose were provided by Sigma-Aldrich Merck (Madrid, Spain) for the chemical experiments. COMSOL Multiphysics 6.1 (Comsol AB, Stockholm, Sweden) was employed for numerical calculations and modelling of the electrical capacitance transient and the flow dynamics of the paper strip in the wicking process. The AC/DC, microfluidics, and porous media flow modules were utilized for the programming of COMSOL applications, including the geometries and materials of the different experimental setups described below. The smartphone application was coded using Android Studio Dolphin (2021.3.1) as the integrated development environment (IDE). The application was designed and tested with Application Programming Interface (API) level 31 (Android 12), although it is compatible with older Android versions, API 22 (Android 5.1) being the minimum level required for functional compatibility. The open-source library MPAndroidChart was used for the visual representation of the data within the application.

Capacitive sensing platform

Our design of the electronic platform for monitoring the dynamics of liquid imbibition in a paper strip is based on tracking the capacitance change over time when wicking the liquid. As depicted in Fig. 2, we have patterned a pair of metal parallel electrodes positioned below the strip in the path of the advancing imbibition front. As the paper strip becomes wet, the capacitance between these electrodes changes, allowing for accurate and real-time measurement of the process without the need for video cameras or external flow sensors. Double-sided adhesive tape is attached between the electrodes and the paper strips to fix both elements, also providing a waterproof barrier to prevent the electrodes from getting wet and causing a short-circuit, since they need to be dry for an accurate and reliable capacitance measurement. Our electronic measurement system lies on the small breadboard Arduino Nano (Chiasso, Switzerland) as the controller unit. This controller was selected for its versatility, low power consumption of 19 mA, light weight of 7 g, wireless communication and battery-powering capabilities. This unit is responsible for the configuration and data analysis of the AD7746 capacitive sensor (Analog Devices Inc., Cambridge, MA, USA), which is a 24-bit, 2-channel capacitive to digital converter employed to measure the capacitance change due to the liquid wicking in the paper strip. This capacitive sensor can measure capacitance at 32 kHz achieving an accuracy of 4 fF with a full-scale range of 8 pF. Moreover, a ±4 pF capacitance offset can be added to adjust

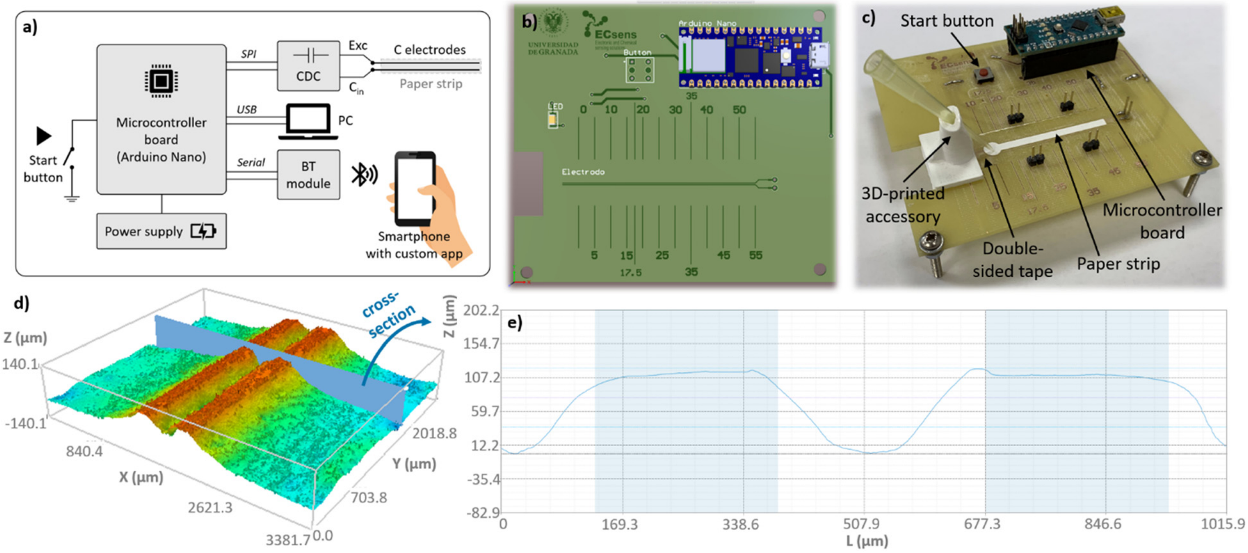

Fig. 2 Capacitive sensing platform. (a) Electronic schematic; (b) PCB layout; (c) photo including paper strip and accessory for repetitive water intake; (d) 3D profiler image of the capacitive sensing electrodes; (e) actual cross-section of the electrodes.

the measuring range. Sampling frequency can also be selected from 10 to 90 Hz, and its communication with the controller is *via* I^2C serial interface. An on-chip temperature sensor is also included with a resolution of 0.1 °C and accuracy of ±2 °C. The acquired data can be sent wirelessly to the user *via* Bluetooth with a low power and reprogrammable BM78 Bluetooth module (Microchip Tech. Inc., Chandler, AZ, USA). Wired USB bus is also available to display the data on any serial monitor of a computer for debugging purposes.

As shown in Fig. 2b, the pair of metal parallel electrodes were fabricated on a standard copper clad FR4 board, where the electronic components and systems (Arduino Nano, capacitive sensor, and Bluetooth module) were soldered. Considering the practical minimum spatial resolution of the circuit board plotter, the two metal electrodes were initially designed with a width and separation of 254 μm, and a total length of 45 mm. Because of the tolerance of the PCB plotter, the actual width and gap electrodes were measured using an optical profilometer as shown in Fig. 2d and e, whose details are given in Table 1. The copper layer thickness of the FR4 board determined the electrode thickness, which was 35 μm. With this configuration, the measured capacitance of the nude electrodes was 1.71 ± 0.01 pF. In addition, the designed printed circuit board includes a button for manual data acquisition initialization and a patterned ruler for quick localization of the imbibition liquid front on the paper strip.

The paper strip is attached to the sensing platform in horizontal position; therefore, the gravity effect is not considered in this work. Firstly, a strip of double-sided adhesive tape with dimensions of 10 mm width and 50 mm length is centred and aligned on the capacitive electrodes. This layer functions as a liquid barrier between the electrodes and the paper strip, ensuring that the paper strip remains fixed and flat. Subsequently, the paper strip is attached to the tape with the same centred and aligned position along the longitudinal axis (x-axis) of the electrodes pair (refer to

Table 1 Dimensions and electrical parameters of capacitance *versus* the length of the liquid front simulation for our measurement platform

Structure (material)	Parameter	Value
Substrate (FR4)	Thickness	1.5 mm
	Relative permittivity	4.5
Electrodes (Cu)	Width[a]	200 μm
	Gap[a]	300 μm
	Thickness	35 μm
Double-sided adhesive tape (polypropylene)	Thickness[a]	75 μm
	Relative permittivity	2.4
Paper (Whatman G1)	Total length	40/45 mm
	Width	3/5 mm
	Thickness[a] (dry)	180 ± 2 μm
	Relative permittivity[b] (dry)	1.9 (ref. 40)
	Thickness[a] (wet)	230 ± 5 μm
	Relative permittivity[b] (wet)	18

[a] Measured with the profilometer. [b] Measured with the impedance analyser.

Fig. 2c). In order to ensure high test reproducibility, it is essential to precisely control the liquid volume and the water intake disposition, since prior research has proved that the initial contact between the liquid and the paper is a critical determinant of flow rate.[3,39] To achieve this objective and in line with the typical use of this kind of paper strip in analysis, a polymeric accessory has been designed and fabricated using 3D printing technology to secure the micropipette tip in a fixed position. Firstly, a controlled liquid volume is aspired by the micropipette and deposited in the tip. Then, the tip is detached from the micropipette body and brought into contact with the zone of the paper liquid intake. As we will show below, our tests demonstrate that the proposed setup ensures that the liquid flows reproducibly into the paper, driven by the capillary pressure.

Measurement procedure. The procedure for measuring capacitance as a function of time, $\Delta C_{\mathrm{exp}}(t)$, is illustrated in the flow diagram presented in Fig. S1 of the ESI† file. Upon powering up the system, the Arduino Nano configures the capacitive sensor by selecting the desired channel (A or B), the sampling rate, continuous or single conversion mode, and the offset to adjust the measurement range. To minimize electric noise, a sampling rate of 16 Hz was selected to filter out the 50 and 60 Hz electric noise, continuous conversion, and an offset to measure capacitance ranging from 0 to 8 pF. Subsequently, upon pressing the start button, the controller verifies whether the final conversion flag is enabled to store the read capacitance value until the configured output time is reached. To improve the signal-to-noise ratio, a moving average filter of 5 consecutive samples is implemented in the Arduino sketch, providing valid capacitance readings every 100 ms. Following numerous tests, this configuration has provided stable and accurate capacitance measurements for this study. Finally, the data is transmitted *via* Bluetooth and USB to a smartphone and a computer, respectively. The description of the custom-developed smartphone application along with some screenshots are included in Fig. S2.†

Numerical analysis

In this study, a finite element method (FEM) was used to solve the numerical problem using the COMSOL Multiphysics environment. A dual simulation was carried out, where the capacitance (C) of the electrodes under the paper strip was first calculated as a function of the length of the liquid front assuming a step function for the transition between dry paper and wet paper. To achieve this, the total paper length (L) was divided into ten equal segments, and the electrical capacitance of the entire paper strip was calculated sequentially with the complete paper dry, then with the initial segment wet, and so on until all ten segments were completely wet. This provided the simulated capacitance as a function of the length of the liquid front, $\Delta C_{\mathrm{sim}}(L_{\mathrm{lf}})$. The AC/DC module was used for this numerical calculation, including the complete platform geometry and relevant electric parameters, which are listed in Table 1. The dimensions were measured with the profilometer (including thickness of the swelled paper, as shown in Fig. 3); the paper permittivity (dry and wet) was determined with the described setup; and the rest of the parameters were taken from the well-known material properties (copper, FR4 that is glass-reinforced epoxy laminate material, and polypropylene). Paper dimensions were analysed, and Fig. 3a–c shows a noticeable increase in paper thickness while wicking, measuring approximately 50 μm of swelling (an additional 27% from the initial dry paper thickness of 180 μm).

Once the correlation between the capacitance and the length of the liquid front was established by electrical simulation, the next step involved incorporating the time variable and liquid flow dynamics into the calculation. Therefore, the second step involved simulating the liquid

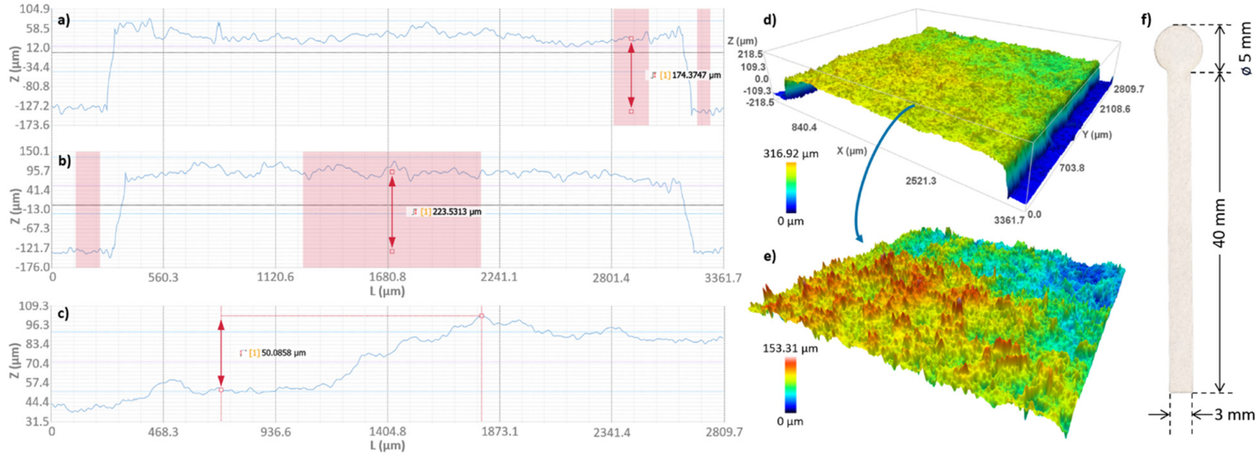

Fig. 3 Paper swelling. (a) Cross-section profile measured in the dry area; (b) cross-section profile measured in the wet area; (c) cross-section profile of the transition from dry to wet areas; (d) 3D profiler image of the paper, including the substrate; (e) detailed 3D profiler image of the paper without the substrate; (f) photograph of the paper strip with dimensions, consisting of a circular zone for liquid intake, followed by a rectangular zone for liquid imbibition.

flow, where the length of the liquid front, $L_{\mathrm{lf}}(t)$, intake volume, and flow rate, $Q(t)$, were calculated as a function of time. In this simulation, the paper strip was initially considered filled with air with an initial water saturation of 0.01. The Brooks and Corey model for capillary pressure and relative permeabilities was used for the time-dependent simulation.[41] No water flow was allowed at the side boundaries of the paper strip. The boundary conditions for the bottom and top boundaries for Darcy's law were the atmospheric pressure for water phase at the bottom, and the hydrostatic atmospheric pressure minus the capillary pressure at the top. For the phase transport, no flux was assumed for the air phase at the bottom boundary. At the top boundary, a mass flux for the air phase was defined, resulting from the pressure gradient given in the Darcy's model.

This numerical calculation employs the multiphase flow in porous media, which couples the Darcy's law and Phase Transport in Porous Media interfaces. The effect of evaporation was not considered, as explained below in the Experimental setup subsection. The Phase Transport in Porous Media interface follows separate equations for the volume fraction s_i of the wetting or nonwetting fluid i:

$$\frac{\partial}{\partial t}\left(\varepsilon_{\mathrm{p}}\rho_i s_i\right)+\nabla\cdot\left(-\rho_i\kappa\frac{\kappa_{\mathrm{r}i}}{\mu_i}\left(\nabla p_i\right)\right)=0, \tag{1}$$

where ε_{p} is the porosity, κ is the permeability, $\kappa_{\mathrm{r}i}$ is the relative permeability (a function of saturation for a given fluid), μ_i is the dynamic viscosity of the fluid, p_i is the pressure, and ρ_i is the fluid density of phase i. As the sum of the volume fractions of the two phases is 1, we can calculate $s_1 = 1 - s_2$. For the wetting phase, the used equations are:[41]

$$p_{\mathrm{c}}=p_{\mathrm{ec}}s_1^{\frac{-1}{\lambda_{\mathrm{p}}}} \tag{2}$$

$$\kappa_{\mathrm{r}1}=s_1^{3+\frac{2}{\lambda_{\mathrm{p}}}} \tag{3}$$

$$\kappa_{\mathrm{r}2}=s_2^2\left(1+s_1^{1+\frac{2}{\lambda_{\mathrm{p}}}}\right) \tag{4}$$

$$p_{\mathrm{ec}}=\frac{2\gamma\cos\cos\theta}{R_{\mathrm{c}}} \tag{5}$$

where p_{c} is the capillary pressure, and p_{ec} is the entry capillary pressure.[42] Moreover, λ_{p} is the pore size distribution index, and γ is fluid surface tension. We consider 0° static contact angle as usual in studies with water,[16] and the initial value of the volume fraction s_2 as 0.99. Additionally, we incorporated to this standard modelling the effects of observed porosity and pore size reduction, which are known to be significant factors in the swelling of porous media.[10,11] To this end, we included the following relationships to account for the parameter dependence on these magnitudes:

$$R_{\mathrm{C}} = R_{\mathrm{c0}}(1 - \alpha\cdot t) \tag{6}$$

$$\varepsilon_{\mathrm{p}} = \varepsilon_{\mathrm{p0}}(1 - \alpha\cdot t)^2 \tag{7}$$

$$\kappa \propto \varepsilon_{\mathrm{p}}R_{\mathrm{c}}^2 = \kappa_0(1 - \alpha\cdot t)^4 \tag{8}$$

where parameters with subscript 0 refer to the initial values, and α is the pore size reduction coefficient (s^{-1}). We are assuming a functional dependence of permeability with the pore size as the capillary-model.[43] The parameters used in this second simulation step are listed in Table 2 for the two liquids employed in the experiments.

To demonstrate the impact of including on the flow dynamics the pore size reduction resulting from paper swelling, Fig. S3† shows the absorbed water mass for a range of α values from 0 to $2 \times 10^{-3}\ \mathrm{s}^{-1}$. As expected, a significant variation can be observed in the wicking dynamics with this coefficient, even at low intervals such as 20 s. As we demonstrate later, our best fitting with experimental data is given for $\alpha = 10^{-3}\ \mathrm{s}^{-1}$. This value is consistent with a similar coefficient of $\alpha = 0.954 \times 10^{-3}\ \mathrm{s}^{-1}$ reported in a previous study.[11]

Following the numerical simulation, a conclusive relationship between the experimental capacitive transients and the flow dynamics was established. As a result, the numerically calculated volume/mass intake and flow rate will be derived as a function of time from the experimental capacitance transient during the wicking process, as detailed in the Results section. The only free parameter is the initial paper permeability, κ_0, with the value presented in Table 2 being compatible and intermediate with those reported by the capillary-model ($\kappa_0 = 2.5 \times 10^{-12}\ \mathrm{m}^2$)[43] and the manufacturer ($\kappa_0 = 9.8 \times 10^{-14}\ \mathrm{m}^2$), and the value referred in recent studies.[47] Numerous empirical and theoretical models have reported varying values for this parameter.[11,48] However, a comprehensive discussion regarding this issue is outside the scope of this work.

Another crucial issue that needs to be considered is the impact of the inaccuracies in the values of the properties presented in Tables 1 and 2 on the calculation of the flow parameters (intake volume and flow rate). To examine the relative sensitivities of the flow monitoring parameters as a function of these properties, we conducted numerical calculations as described in the ESI† and outlined in Fig. S4. By introducing separate relative variations of approximately ±10% for the initial porosity ($\varepsilon_{\mathrm{p0}}$), wet paper thickness ($\mathrm{th_w}$), and initial permeability (κ_0), we determined the corresponding variations in volume and flow rate over time. Through a comparison of the three curves associated with each property, it can be concluded that these relative variations are also reflected in the flow parameters for initial porosity and paper thickness. Therefore, relative sensitivities of 1 were obtained for $\varepsilon_{\mathrm{p0}}$ and $\mathrm{th_w}$. On the other hand, the flow parameters exhibited a relatively low sensitivity to variations in the initial permeability, with a sensitivity of 0.4 for volume variation and 0.11 for flow rate variation. This calculation demonstrates that our procedure exhibits greater robustness against inaccuracies in the only free parameter considered in our simulations (*i.e.*, the initial permeability) compared to the other studied properties.

Table 2 Parameters for the liquid wicking simulations

	Value	
Parameter	Purified water	1 M NaCl aqueous solution
Surface tension (γ)	0.0723 N m^{-1}	0.069 N m^{-1} (ref. 44)
Viscosity (μ)	10^{-3} Pa s	1.09 10^{-3} Pa s[45]
Density (ρ)	1000 kg m^{-3}	927 kg m^{-3}[a]
Pore size reduction coeff. (α)	10^{-3} s^{-1}	
Pore distribution index (λ_p)	2	
Initial pore radius (R_{C0})	5.5 μm	
Initial porosity (ε_{p0})	0.66 (ref. 46)	
Initial permeability (κ_0)	4.4 10^{-13} m^2	
Air density	1 kg m^{-3}	
Air viscosity	1.76×10^{-5} Pa s	

[a] Measured at 21 °C.

Experimental setups

The measurements were conducted in our laboratory under controlled environmental conditions of 21 ± 1 °C temperature and 30 ± 10% relative humidity. An estimation of the evaporation effect on the liquid wicking dynamics was calculated using these ambient conditions along with the flow parameters presented in Table 2 according to a previously reported model.[24] We obtained a correction of the wicking duration below 1% and 2% for time intervals of 40 and 90 s, respectively. As a result, the influence of liquid evaporation on our experiments can be neglected for wicking times below 60 s, and this effect was not considered in the numerical simulations.

Firstly, we measured the relative permittivity of dry, ε_r(dry), and wet samples, ε_r(wet), Whatman G1 paper samples. To perform this measurements, six circular-shaped paper samples with 6 cm diameter (three dry and three wet) were laser-cut and inserted between the type A electrodes of the 16451B test fixture, which was connected to the 4294A impedance analyzer. Our results showed ε_r(dry) = 1.75 ± 0.15, which agrees with a recent experimental finding of 1.9 measured by microwave reflection.[40] Additionally, we determined ε_r(wet) = 18 ± 2 for wet paper, and this value was used in the numerical calculation of the capacitance (see Table 1). The uncertainty in both cases was calculated as the standard deviation of the experimental dataset. Two preliminary validation experiments were conducted:

V1. Validation of the experimental capacitance measurements. For this purpose, we compared the capacitance values obtained with the developed sensing platform with those measured from the LCR meter used as reference system. To do this, three paper strips with a circular zone of 5 mm diameter for liquid intake, followed by a rectangular zone with dimensions of 40 mm length and 3 mm width for liquid imbibition, were laser-cut as shown in Fig. 3f. After attaching these strips to the capacitive platform, they were imbibed with the liquid according to the procedure detailed above. During the validation, the LCR meter was connected to the platform electrodes so that the measurements were conducted under the same conditions. The capacitance measurements were taken by switching between both systems due to the capacitance input coupling of the reference system, which saturated the AD7746 sensor of the platform. The dependence with the temperature of the capacitive platform was also measured from 15 to 35 °C.

V2. Validation of the simulated capacitance. Using the video camera of the mentioned smartphone along with the rule patterned on the PCB (see Fig. 2), we measured the capacitance increase as a function of the length of the liquid front (L_{lf}) of three paper strips. Numerical capacitances were also calculated as a function of L_{lf} by the electrical simulation, using the parameters presented in Table 1. The experimental capacitance registered by the developed measurement platform was then compared to the calculated numerical capacitances.

Next, a series of experimental tests were planned to evaluate the performance of the flow monitoring platform in various scenarios, including a reproducibility test, control flow with different paper strip geometries, flow retention with chemical valves, and an application of flow monitoring for accurate analytical determination.

T1. Reproducibility tests with purified water and a 1 M NaCl aqueous solution. For each liquid, five paper strips were used as described in V1. Uncertainty was calculated as the standard deviation of the dataset.

T2. Dependence of paper strip geometry on flow dynamics. Paper strips with exponentially varying width were prepared to modulate the filling dynamics.[39] In this case, the initial paper width was w_0 = 5 mm, and the total length L = 45 mm. The variable width was defined as $w(x) = w_0 e^{-x/l_0}$. Replicating the experiment previously proposed,[39] with $w(x) = W_0$, and $l_0 = L/2$ and $L/3$, the flow dynamics of three strip patterns were analysed with the capacitive platform.

T3. Flow retention with chemical valves. A couple of simple experiments including chemical valves were carried out to evaluate the platform's ability to measure irregular flows. Wax, chitosan and sucrose were used as barriers in the imbibition filling with purified water, using the same paper strip shape of experiment V1.

T4. Flow time control for colorimetric determination. An experiment was conducted to assess the performance of the platform in colorimetric detection, where reaction time is an essential parameter to ensure accurate colour measurement. GJM-530 dye was covalently immobilized on Whatman grade 1 paper sheets.[49] These sheets were then cut using a punch into 0.5 cm diameter circles and stored under light-protected from light. Using double-sided tape, the circles were affixed to the end of the paper strip positioned over the flow controller. To initiate the reaction, 28 μL of 0.1 M phosphate buffer solution was added to the intake zone. The reaction was tested under a fixed pH value of 10, resulting in a color change of the dye to red.

Results and discussion

Experimental validation

V1. Validation of the experimental capacitance measurement. Excellent agreement between both capacitive registers can be observed in Fig. 4a. A full-scale (8 pF) relative error of 0.25% was measured, resulting in an absolute capacitance error of ±0.01 pF. This error becomes ±0.014 pF when ΔC is calculated.

Moreover, the temperature sensor integrated into the capacitive detector was utilized to characterize the linear temperature coefficient, α_T, within the temperature range of 15 to 35 °C. An average value of $\alpha_T = 0.6$ fF K^{-1} was obtained. This low thermal drift ensures the reliability of capacitance data under typical testing conditions.

V2. Validation of the numerical capacitance

Fig. 4b compares the experimental and simulated capacitances, showing an excellent agreement with no free parameter in the numerical simulation (see Table 2). With this comparison, we consider that our capacitive platform can provide reliable data, and no further video recordings will be required in subsequent experiments. Moreover, a linear trend was obtained with the length of the liquid front, validating the step approximation for the liquid front as a suitable assumption. This linear fitting allows the determination of L_{lf} from the capacitive measurements through a simple proportionality constant. This fact will provide the link to calculate the absorbed mass/volume and flow rate, $Q(t)$, in the paper strip from the measurements of the proposed platform. The flow chart in Fig. 4c details the procedure, which involves the following steps:

1. Experimental $\Delta C_{\mathrm{exp}}(t)$ and $\Delta C_{\mathrm{exp}}(L_{\mathrm{lf}})$ are registered by our capacitive platform. The latter is performed only once for validation purposes.

2. The numerical calculation of capacitance increment with L_{lf} is performed, $\Delta C_{\mathrm{sim}}(L_{\mathrm{lf}})$, and it is fitted with $\Delta C_{\mathrm{exp}}(L_{\mathrm{lf}})$.

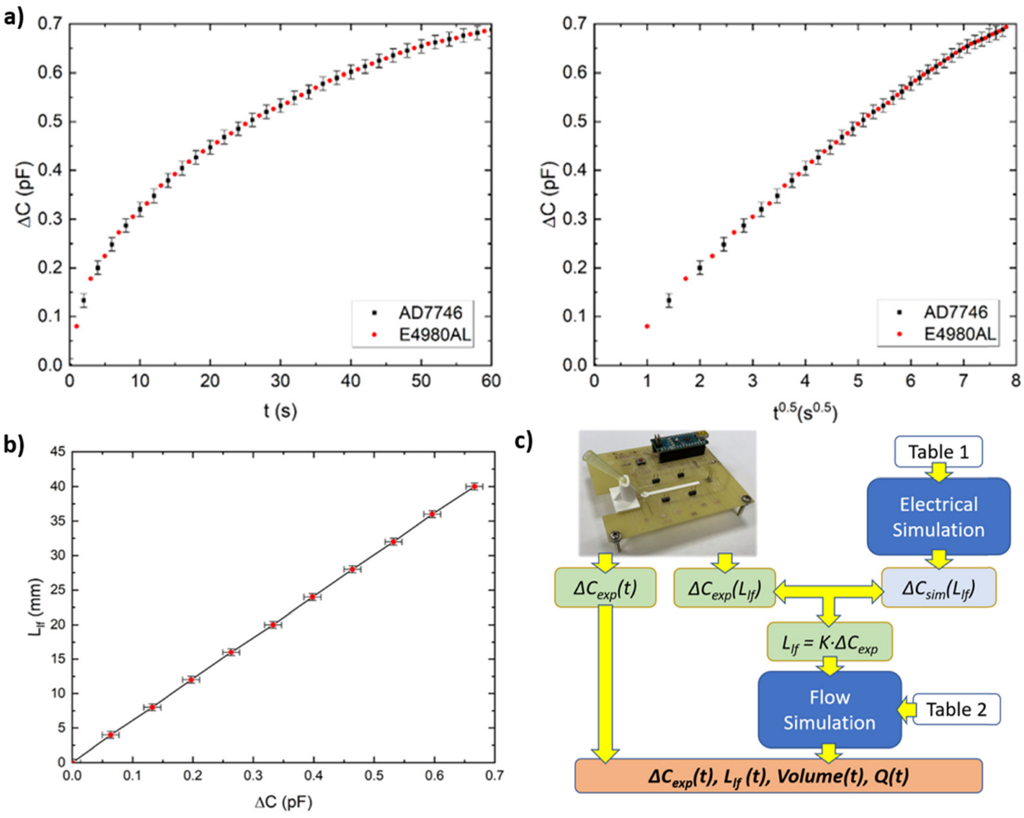

Fig. 4 (a) Validation test curves: comparison between proposed AD7746 capacitive sensor (black symbols) and the reference instrument E4980 (red symbols) *versus* time and square root of time. (b) Comparison of the experimental data (symbols) and numerical simulation (line), also showing the linear correlation between the length of the liquid front and the capacitance change. (c) Experimental/numerical procedure of flow monitoring.

The simulation includes the platform geometry and electrical parameters, which are checked with this fitting.

3. Using the mentioned linear relationship between the capacitance increment and the length of the liquid flow, $L_{\mathrm{lf}} = K\Delta C_{\mathrm{exp}}$, (where K is a proportionality constant), this capacitance is transformed into the experimental length of the liquid front as a function of time, $L_{\mathrm{lf}}(t)$.

4. This magnitude is compared with the COMSOL calculation of the flow dynamics, where magnitudes such as length of liquid front, $L_{\mathrm{lf}}(t)$, absorbed mass/volume, and flow rate, $Q(t)$, are numerically calculated.

5. From the fitting between the experimental and numerical lengths of the liquid fronts, the volume and flow rate are also obtained as a function of time, displaying such flow parameters as results on the smartphone. As mentioned above, only the permeability value is a fitting parameter in this numerical calculation. The rest of the geometry, electrical, and flow parameters were measured or provided by manufacturers and previous literature.

Monitoring system performance

T1. Reproducibility tests. To demonstrate the reproducibility of the microfluidic platform, five replications of experiments were performed with two different aqueous solutions under the aforementioned conditions. The standard deviation of the measurements is shown in Fig. 5 as a grey area under the red line (experimental tests). The maximum uncertainty obtained for purified water was 0.024 pF (0.5 μl) and 0.00036 pF s^{-1} (9 nl s^{-1}) in the case of flow rate. The error for NaCl 1 M was slightly higher in ΔC, 0.03 pF (0.7 μl), and 0.0003 pF s^{-1} (7 nl s^{-1}) for flow rate determination. As can be seen, the results obtained by simulation with COMSOL (symbols) show good agreement with the experimental results.

T2. Geometric flow control. To investigate the impact of paper geometry on liquid flow, Elizalde *et al.*,[39] designed paper strips of lengths *L*, *L*/2 and *L*/3, as described in their work. The *L*/4 structure was excluded from the study as the tip of the paper in the narrowest end was located between the platform electrodes, rendering reliable testing impossible. Both experimental data and COMSOL simulations indicate similar tendencies and behaviour as those presented in the mentioned study,[39] as shown in Fig. 6. Notably, the strip with the smallest exponential width geometry exhibited a shorter total filling time of the paper.

T3. Chemical valves. With the purpose of investigating variations of flow conditions along paper strips, several custom-made chemical valves were tested. First, 5 μl of 25 mg ml^{-1} chitosan in purified water were deposited onto a paper strip, allowing it to dry for 40 minutes prior to testing. As shown in Fig. 7a, a slight delay in flow rate was observed

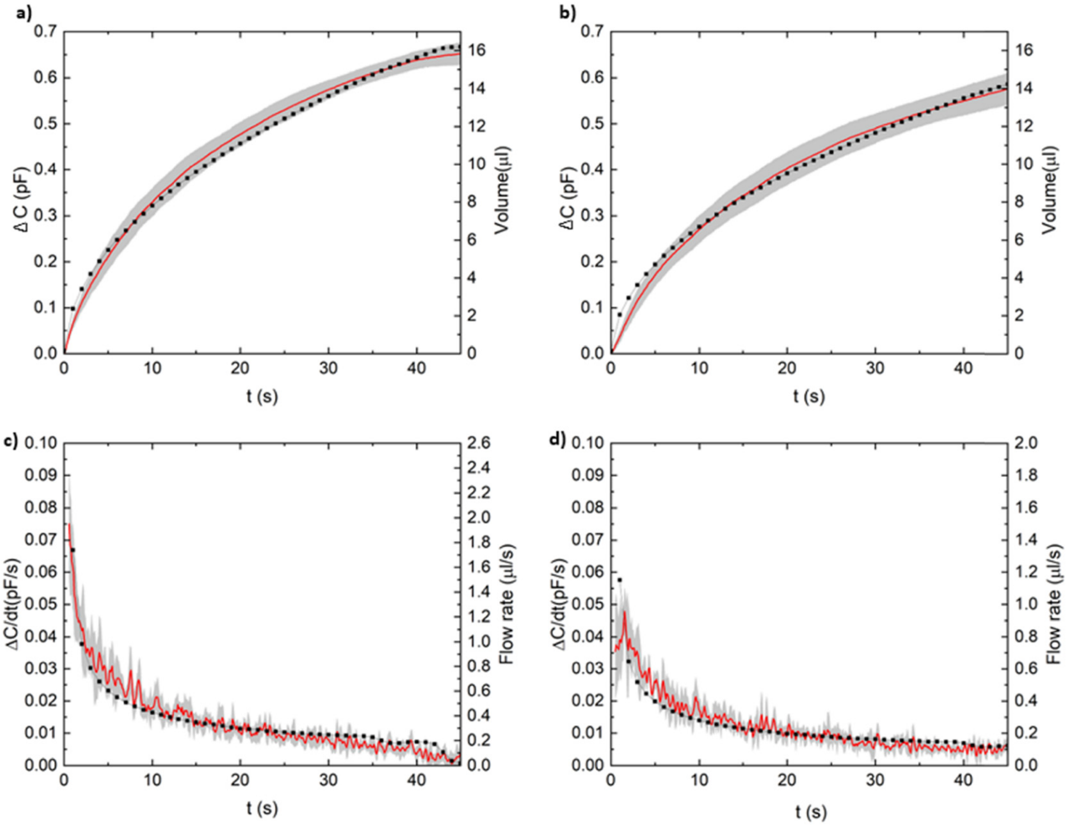

Fig. 5 Purified water (a and c) and 1 M NaCl solution (b and d) wicking dynamics (capacitance/volume variation and flow rate): experimental data (line) and numerical simulations (symbols). The grey area under the line represents the experimental standard deviation of dataset.

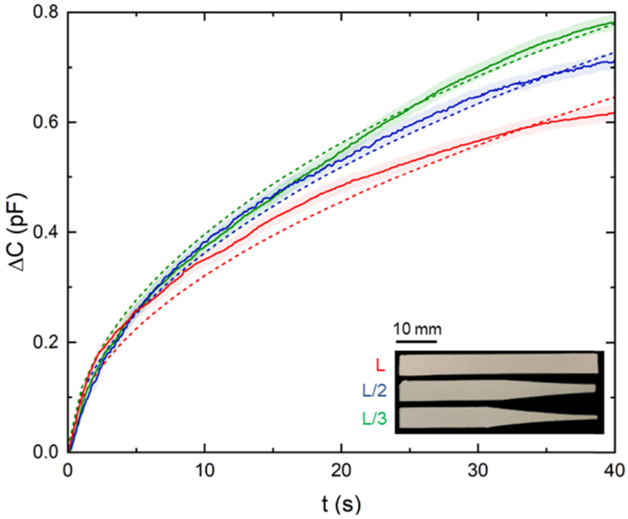

Fig. 6 Geometrically flow control for *L*, *L*/2 and *L*/3 paper strips: experimental data and error (lines and coloured area) and numerical simulation (dashed lines).

from seconds five to seven due to the physical barrier created by the chitosan. The second valve tested was created by using a common red crayon, which diffused the wax across the strip creating a barrier after being heated at 100 °C for five minutes. As shown in Fig. 7b, this barrier completely halted the flow of the liquid solution until it was heated again at 80 °C for two minutes, after which the flow rate was increased.

Finally, we investigated the use of a sucrose solution as a valve to slow-down the flow rate in our microfluidic platform. In order to construct an efficient barrier, three layers of 4 μl of saturated sucrose in purified water were deposited, allowing each layer to dry for 20 minutes before depositing the next, and allowing a complete day for the last deposition to dry. A decrease in the flow rate of the liquid between 9 to 17 seconds can be observed in Fig. 7c. Therefore, our capacitive measurement system for paper-strips has successfully demonstrated to accurately monitor both the forward movement and flow rate of liquid solutions, providing information on the position of the liquid front of various reagents that may be utilized in more complex chemical reactions. Furthermore, it would be feasible to monitor the time required for a solution to cross over a previously placed reagent, to ensure the complete reaction before measuring the target information.[5]

T4. Flow time control for colorimetric determination. This test demonstrated the capability of the proposed platform for taking accurate analytical measurements through flow monitoring. When the phosphate buffer solution was placed in the paper strip's intake area, several facts can be pointed out according to Fig. 8. As can be seen, the real-time monitoring of capacitance exhibited a change in slope upon the solution's arrival at the detection area (t_A). Subsequently, at t_B, the detection area became fully saturated, resulting in a constant capacitive response. At this moment, a timer was set for 60 s to ensure reaction stabilization before colour detection at t_C. In this case, a 60 s stabilization period proved to be an optimal time to yield a stable response.[49]

Discussion

We have presented a capacitive sensing platform for flow monitoring in capillary-driven microfluidic devices, specifically demonstrated for μPADs. This proposed system is characterised for its compactness and reusability, utilizing off-the-shelf electronics and fabricated on a printed circuit board. In contrast to alternative solutions, no external or bulky equipment or sensors are required. Furthermore, by incorporating commercially available batteries, the system can operate independently of a computer connection. Configuration of the system and retrieval of data are wirelessly performed using a smartphone, enabling real-time

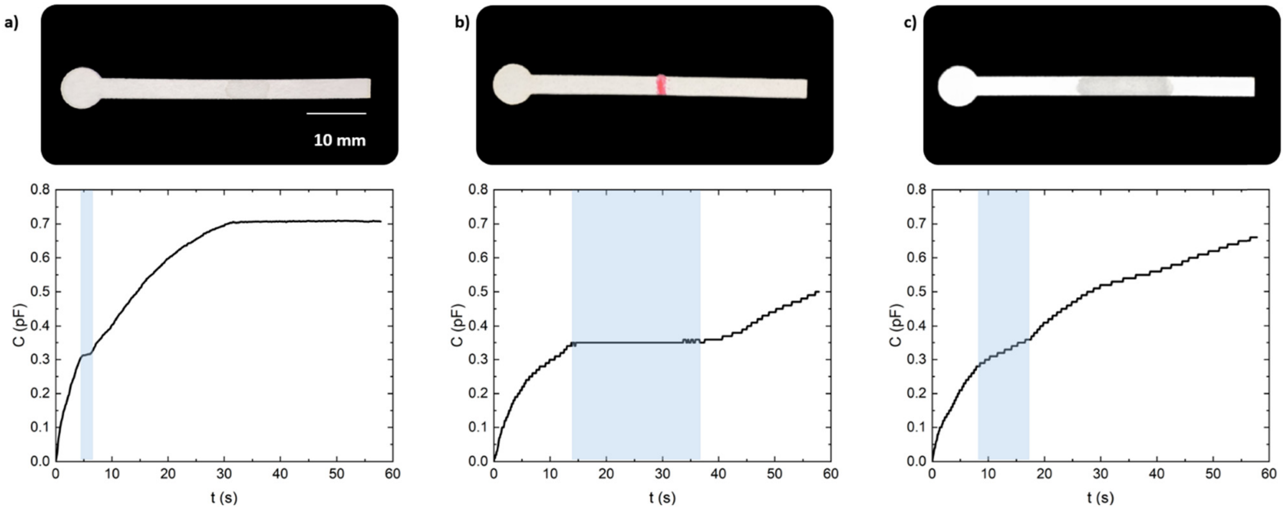

Fig. 7 Experimental capacitive transients using different chemical valves. Top pictures show the paper strip with the deposited chemicals: a) chitosan, b) wax barrier (heated after 23 seconds), and c) sucrose. Experimental errors have not been represented for the sake of clarity.

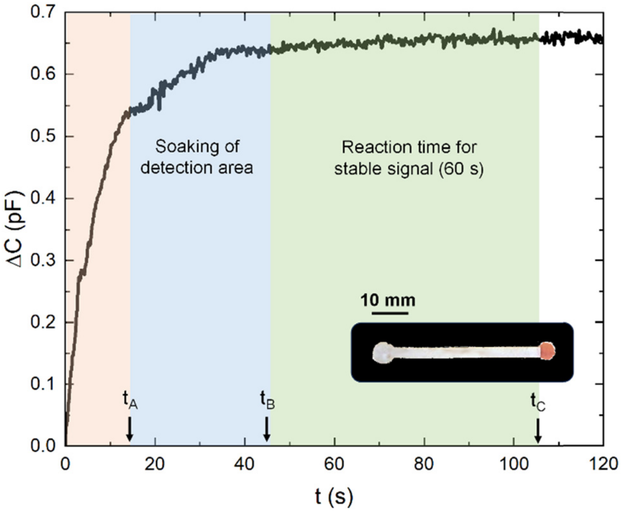

Fig. 8 Experimental capacitance transient of the T4 test, monitoring the imbibition of the paper strip (orange zone), the wetting of the detection area (blue zone), and the duration of 60 s for the complete colorimetric reaction and accurate colour measurement. The limit times between these periods are denoted as t_A, t_B, and t_C. The inset shows the paper strip with the coloured dye.

and on-site measurement of liquid flow in paper strips. The smartphone application facilitates system operation by non-trained users through a user-friendly and intuitive interface that guides users through the microfluidic tests.

To acquire comprehensive information about the flow process, the capacitive measurements need to be initially combined with numerical simulation, including the physical and chemical parameters that characterize the liquid and the paper strip. However, once the numerical constants establishing the relationship between capacitance and flow parameters (intake liquid volume and flow rate) are determined, the platform can be readily utilized for subsequent tests without the need for further simulations, as long as the liquid and paper strip geometry remain unchanged.

Integrated electrodes for detection or liquid manipulation have already been employed in microfluidic devices for electrokinetic flow, electrowetting, or conductivity monitoring,[50] exhibiting excellent performance for local actuation or sensing. Moreover, within our developed versatile flow monitoring platform, the paper substrate could be substituted with fabric, as the capacitive sensing transduction principle will respond to changes in the dielectric constant of a wet fabric. Additionally, by adding more digital capacitance detector chips, the system can be scaled, enabling flow monitoring not only in basic paper strips but also in different paper-based patterns with multiple liquid paths, thereby expanding the capabilities of the system. Therefore, drawing inspiration from our previous expertise in planar printed capacitive sensors and the system presented by Temiz *et al.*,[26] our work introduces several remarkable innovations: i) incorporation of a high-resolution digital capacitive detector with a built-in temperature sensor, ii) application to paper strips, iii) validation of measurements and determination of flow parameters through a physical-based numerical simulator, and iv) easy scalability for multiple paper paths and applicability to fabric substrates.

Conclusions

This work presents a wireless and portable electronic platform designed to monitor the flow and flow rate of liquids in paper-based microfluidic devices driven by capillary force. The full hardware and software tools have been described, and operational specifications have been extracted. Relevant features of this measurement system include its affordability, reusability, and its potential for extension to textile substrates as well. Furthermore, the experimental setup demonstrated notable repeatability and good performance for different paper geometries and chemical valves. Not only qualitative but also quantitative flow and flow rate measurements can be obtained together with numerical simulations of the electrical and flow dynamic phenomena. To achieve this, knowledge of the dielectric constant of the wet paper and flow parameters of the paper and liquid is required, which is the main limitation of this study. Nonetheless, we consider that this information, which is easily accessible, is required to obtain such quantitative information. This fact provides the possibility to deepen in the study of the flow dynamics on paper, an issue still opened to further study and modelling. On the other hand, smartphone have been demonstrated once again as essential and versatile widespread devices capable of visualizing and sharing results, serving as the user-interface for the developed platform.

Author contributions

Conceptualization: A. J. P., N. L. R., I. R. G., P. E., formal Analysis: P. E., L. F. C. V., M. A. C., A. J. P., N. L. R., funding acquisition: A. J. P., L. F. C. V., methodology: all authors, software: I. R. G., P. E., N. L. R., validation: all authors, writing – original draft and writing – review & editing: I. R. G., P. E., L. F. C. V., A. J. P., N. L. R. All authors have read and agreed to the published version of the manuscript.

Conflicts of interest

There are no conflicts to declare.

Acknowledgements

This work was funded by Spanish MCIN/SRA State Research Agency/10.13039/501100011033/ (Projects PID2019-103938RB-I00, ECQ2018-004937-P and grant IJC2020-043307-I) and Junta de Andalucía, Spain, (Projects B-FQM-243-UGR18, P18-RT-2961). The projects and the grant were partially supported by European Regional Development Funds (ERDF) and by European Union NextGenerationEU/PRTR.

References

1 R. Lucas, *Kolloid-Z.*, 1918, **23**, 15–22.
2 E. W. Washburn, *Phys. Rev.*, 1921, **17**, 273–283.
3 A. Böhm, F. Carstens, C. Trieb, S. Schabel and M. Biesalski, *Microfluid. Nanofluid.*, 2014, **16**, 789–799.
4 N. Walji and B. D. MacDonald, *Micromachines*, 2016, **7**, 73.
5 E. Fu and C. Downs, *Lab Chip*, 2017, **17**, 614–628.
6 Y. Yang, E. Noviana, M. P. Nguyen, B. J. Geiss, D. S. Dandy and C. S. Henry, *Anal. Chem.*, 2017, **89**, 71–91.
7 H. Darcy, *The Public Fountains of the City of Dijon*, Paris, 1856, vol. 647.
8 M. Hamdaoui, F. Fayala and S. Ben Nasrallah, *J. Appl. Polym. Sci.*, 2007, **104**, 3050–3056.
9 N. Fries, K. Odic, M. Conrath and M. Dreyer, *J. Colloid Interface Sci.*, 2008, **321**, 118–129.
10 D. Schuchardt and J. Berg, *Wood Fiber Sci.*, 1991, **23**, 342–357.
11 R. Masoodi and K. M. Pillai, *AIChE J.*, 2010, **56**, 2257–2267.
12 S. Chang and W. Kim, *J. Fluid Mech.*, 2020, **892**, A39.
13 L. A. Richards, *Physics*, 1931, **1**, 318.
14 R. Masoodi, H. Tan and K. M. Pillai, *AIChE J.*, 2011, **57**, 1132–1143.
15 D. Rath, N. Sathishkumar and B. J. Toley, *Langmuir*, 2018, **34**, 8758–8766.
16 S. Patari and P. S. Mahapatra, *ACS Omega*, 2020, **5**, 22931–22939.
17 S. Modha, C. Castro and H. Tsutsui, *Biosens. Bioelectron.*, 2021, **178**, 113026.
18 L. Gervais, N. De Rooij and E. Delamarche, *Adv. Mater.*, 2011, **23**, H151.
19 G. G. Morbioli, T. Mazzu-Nascimento, A. M. Stockton and E. Carrilho, *Anal. Chim. Acta*, 2017, **970**, 1–22.
20 H. Lim, A. T. Jafry and J. Lee, *Molecules*, 2019, **24**, 1–32.
21 E. Noviana, T. Ozer, C. S. Carrell, J. S. Link, C. McMahon, I. Jang and C. S. Henry, *Chem. Rev.*, 2021, **121**, 11835–11885.
22 Anushka, A. Bandopadhyay and P. K. Das, *Eur. Phys. J.: Spec. Top.*, 2022, **123**, 1–35.
23 R. J. Roberts, T. J. Senden, M. A. Knackstedt and M. B. Lyne, *J. Pulp Pap. Sci.*, 2003, **29**, 123–131.
24 C. K. Camplisson, K. M. Schilling, W. L. Pedrotti, H. A. Stone and A. W. Martinez, *Lab Chip*, 2015, **15**, 4461–4466.
25 M. N. Islam, J. W. Yost and Z. R. Gagnon, *Analyst*, 2022, **147**, 587–596.
26 Y. Temiz and E. Delamarche, *Sci. Rep.*, 2018, **8**, 1–11.
27 C. Delaney, P. McCluskey, S. Coleman, J. Whyte, N. Kent and D. Diamond, *Lab Chip*, 2017, **17**, 2013–2021.
28 N. Noeth, S. S. Keller and A. Boisen, *Sensors*, 2014, **14**, 229–244.
29 A. Alfadhel, B. Li, A. Zaher, O. Yassine and J. Kosel, *Lab Chip*, 2014, **14**, 4362–4369.
30 L. Zhang, X. Yu, S. You, H. Liu, C. Zhang, B. Cai, L. Xiao, W. Liu, S. Guo and X. Zhao, *Appl. Phys. Lett.*, 2015, **107**, 242901.
31 Z. Zhang, J. Pan, Y. Tang, Y. Xu, L. Zhang, Y. Gong and L. Tong, *Lab Chip*, 2020, **20**, 2572–2579.
32 M. H. Zarifi, H. Sadabadi, S. H. Hejazi, M. Daneshmand and A. Sanati-Nezhad, *Sci. Rep.*, 2018, **8**, 1–10.
33 E. Skotadis, E. Aslanidis, G. Kokkoris, E. A. Vargkas Kousoulas, A. Tserepi and D. Tsoukalas, *Sens. Actuators, A*, 2022, **344**, 113765.
34 J. Collins and A. P. Lee, *Lab Chip*, 2004, **4**, 7–10.
35 N. Arjmandi, C. Liu, W. Van Roy, L. Lagae and G. Borghs, *Microfluid. Nanofluid.*, 2012, **12**, 17–23.
36 J. Wu and J. Ye, *Lab Chip*, 2005, **5**, 1344–1347.
37 C. Bathany, J. R. Han, K. Abi-Samra, S. Takayama and Y. K. Cho, *Biosens. Bioelectron.*, 2015, **70**, 115–121.
38 M. N. Islam, S. M. Doria, X. Fu and Z. R. Gagnon, *Sensors*, 2022, **22**, 1489.
39 E. Elizalde, R. Urteaga and C. L. A. Berli, *Lab Chip*, 2015, **15**, 2173–2180.
40 A. R. Eldamak and E. C. Fear, *Sensors*, 2018, **18**, 4088.
41 R. H. Brooks and A. T. Corey, *J. Irrig. Drain. Div.*, 1966, **92**, 61–90.
42 R. Masoodi and K. M. Pillai, *J. Porous Media*, 2012, **15**, 775–783.
43 F. L. Dullien, *Fluid Transport and Pore Structure*, New York, 1992.
44 B. R. Bzdek, L. Collard, J. E. Sprittles, A. J. Hudson and J. P. Reid, *J. Chem. Phys.*, 2016, **145**, 054502.
45 J. Kestin, I. R. Shankland and R. Paul, *Int. J. Thermophys.*, 1981, **2**, 301–314.
46 V. P. Mai, C. H. Ku and R. J. Yang, *Microfluid. Nanofluid.*, 2019, **23**, 1–10.
47 N. Koursari, O. Arjmandi-Tash, A. Trybala and V. M. Starov, *Microgravity Sci. Technol.*, 2019, **31**, 589–601.
48 R. Liu, Y. Jiang, B. Li and L. Yu, *Microfluid. Nanofluid.*, 2016, **20**, 1–13.
49 M. J. Arroyo, I. Orbe-Payá, M. Ortega, J. Vilar, D. Gallego, G. J. Mohr, L. F. Capitán-Vallvey and M. M. Erenas, *Sens. Actuators, B*, 2022, **359**, 131549.
50 N. Fukuna, T. Sonsa-ard, N. Chantipmanee, P. C. Hauser, P. Wilairant and D. Nacapricha, *Sens. Actuators, B*, 2020, **339**, 129838.